

Spin-wave propagation in a bilayer of van der Waals magnet and ferrimagnetic insulator

Tengfei Xie(谢腾飞) and Huajun Qin(秦华军)

Citation: Chin. Phys. B, 2025, 34 (**10**): 107202. DOI: 10.1088/1674-1056/addce4
http://cpb.iphy.ac.cn; http://iopscience.iop.org/cpb

What follows is a list of articles you may be interested in

Nonreciprocal microwave-optical entanglement in Kerr-modified cavity optomagnomechanics

Ming-Yue Liu(刘明月), Yuan Gong(龚媛), Jiaojiao Chen(陈姣姣), Yan-Wei Wang(王艳伟), and Wei Xiong(熊伟)
Chin. Phys. B, 2025, 34 (**5**): 057202. DOI: 10.1088/1674-1056/adb735

Magnon-magnon coupling in noncollinear synthetic antiferromagnets

Tengfei Zhang(张腾飞), Quwen Wang(王曲文), Min Chen(陈敏), Jie Dong(董洁), Qian Zhao(赵乾), Zimu Li(李子木), Qingfang Liu(刘青芳), Jianbo Wang(王建波), and Jinwu Wei(魏晋武)
Chin. Phys. B, 2025, 34 (**5**): 057201. DOI: 10.1088/1674-1056/adb26b

A novel monoclinic phase and electrically tunable magnetism of van der Waals layered magnet $CrTe_2$

Qidi Ren(任启迪), Kang Lai(赖康), Jiahao Chen(陈家浩), Xiaoxiang Yu(余晓翔), and Jiayu Dai(戴佳钰)
Chin. Phys. B, 2023, 32 (**2**): 027201. DOI: 10.1088/1674-1056/ac9b37

Role of Ag microalloying on glass forming ability and crystallization kinetics of ZrCoAgAlNi amorphous alloy

A Surendar, K Geetha, C Rajan, and M Alaazim
Chin. Phys. B, 2021, 30 (**1**): 017201. DOI: 10.1088/1674-1056/abb65e

Spin Seebeck effect and spin Hall magnetoresistance in the $Pt/Y_3Fe_5O_{12}$ heterostructure under laser-heating

Shuanhu Wang(王拴虎), Gang Li(李刚), Jianyuan Wang(王建元), Yingyi Tian(田颖异), Hongrui Zhang(张洪瑞), Lvkuan Zou(邹吕宽), Jirong Sun(孙继荣), Kexin Jin(金克新)
Chin. Phys. B, 2018, 27 (**11**): 117201. DOI: 10.1088/1674-1056/27/11/117201

SPECIAL TOPIC — Advanced magnonics

Spin-wave propagation in a bilayer of van der Waals magnet and ferrimagnetic insulator

Tengfei Xie(谢腾飞)[1] and Huajun Qin(秦华军)[1,2,†]

[1] *School of Physics and Technology, Wuhan University, Wuhan* 430072, *China*
[2] *Wuhan Institute of Quantum Technology, Wuhan* 430206, *China*

(Received 24 March 2025; revised manuscript received 14 May 2025; accepted manuscript online 27 May 2025)

Spin waves in van der Waals magnets hold promise for magnonic devices and circuits down to the two-dimensional limit. However, their short decay lengths pose challenges for practical applications. Here, we report on a material platform consisting of a van der Waals magnet, Fe_5GeTe_2 (FGT), and a ferrimagnetic insulator of yttrium iron garnet, $Y_3Fe_5O_{12}$ (YIG), which supports the low-loss propagation of spin waves. Using broadband spin-wave spectroscopy, we observed an increase in spin-wave group velocity with decreasing temperature, which peaks at 30 K in the YIG and FGT/YIG films. This effect is ascribed to a change in the saturation magnetization of YIG and FGT/YIG at low temperature, resulting in a change in the spin-wave dispersion relations. Using micromagnetic simulations, we further investigated spin-wave propagation in an FGT/YIG bilayer and revealed a longer spin-wave decay length in the bilayer than in a single FGT layer, which is due to the lower effective damping in the bilayer. Moreover, asymmetric spin-wave dispersion, induced by a chiral dipolar interaction between the YIG and FGT layers, enables nonreciprocal control of spin-wave propagation.

Keywords: magnonics, spin waves, van der Waals magnets, yttrium iron garnet thin films

PACS: 72.10.Di, 75.50.Gg, 76.50.+g, 96.12.Hg

DOI: 10.1088/1674-1056/addce4 **CSTR:** 32038.14.CPB.addce4

1. Introduction

Two-dimensional (2D) van der Waals (vdW) magnetic materials have attracted tremendous research interest in spintronics and magnonics due to their novel physics and promising applications in device miniaturization into the 2D limit.[1–5] In 2018, layered ferromagnetism was experimentally discovered in CrI_3[6] and $Cr_2Ge_2Te_6$,[7] which overcomes the absence of long-range order in 2D systems predicted by the Mermin–Wagner theorem.[8] This groundbreaking discovery revealed that intrinsic magnetic anisotropy in vdW materials, induced by strong spin–orbit coupling and crystal field effects,[9] enables magnetic order stabilization at atomic-scale thicknesses. Unlike three-dimensional magnetic materials, 2D magnetic systems exhibit strong confinement effects; their restricted geometry not only modulates the spatial distribution of magnetic dipolar or exchange interaction, but also provides a new platform for quantized spin-wave (magnon) transmission,[10] laying the foundation for developing nanoscale magnonic integrated circuits.[11–13]

Ferromagnetic resonance (FMR) and propagating spin waves have been extensively explored in ferromagnetic and antiferromagnetic vdW materials, including CrI_3,[14–16] $CrCl_3$,[17] $Cr_2Ge_2Te_6$,[18] Fe_5GeTe_2,[19,20] and CrSBr,[21] $MnPS_3$.[22] Taking atomically thin CrI_3 layers as an example, their FMR modes[14] and 2D magnons[15] have been observed, which unveiled their magnetic dynamic responses in the gigahertz and terahertz frequency range. Most vdW ferromagnets suffer from high magnetic damping, with a Gilbert damping constant α in the range of 0.01 to 0.05.[16,19] The high magnetic damping arises from magnon–phonon coupling, interfacial defect scattering, and spin fluctuations under dimensional confinement. Recently, spin-pumping measurements on a $Cr_2Ge_2Te_6$ flake showed a low Gilbert damping constant, $\alpha \approx 0.0005$, which supports long-distance spin-wave propagation. The low magnetic damping of $Cr_2Ge_2Te_6$ can be ascribed to two reasons: the absence of spin–electron scattering at low temperatures and a weak spin–orbit interaction. In addition to spin waves in vdW ferromagnets, long-distance magnon propagation,[22,23] magnon valves,[24] electrical tuning of magnon transport,[25] nonlinear coupling,[26] and frequency harmonics[27] have been reported in vdW antiferromagnets, e.g., $FePS_3$, $MnPS_3$, CrSBr, etc. In these studies, direct imaging of spin-wave propagation remains elusive. In 2023, Frank Schulz *et al.* used time-resolved scanning transmission x-ray microscopy to visualize spin-wave propagation in an Fe_5GeTe_2 flake.[20] Their experiments showed that coherent spin waves with short wavelengths of 0.5–1.5 μm have a decay length of about 0.7 μm, which is three orders of magnitude shorter than that of a nanometer-thick YIG film.[28] To advance vdW magnonics, a material platform with a long spin-wave decay length has yet to be demonstrated.

[†]Corresponding author. E-mail: qinhuajun@whu.edu.cn

© 2025 Chinese Physical Society and IOP Publishing Ltd. All rights, including for text and data mining, AI training, and similar technologies, are reserved.

In this article, we integrate high-damping vdW magnets (e.g., FGT) with low-damping magnetic insulators (e.g., YIG) to enhance spin-wave propagation through dynamic interlayer dipolar coupling. Since the damping parameter of FGT in the literature was obtained at low temperature, we measured spin waves in the YIG film and the FGT/YIG bilayer in a temperature range of 300 K to 10 K. Using broadband spin-wave spectroscopy, we observed efficient spin-wave transmission and increased spin-wave group velocity in the films of YIG and FGT/YIG when the temperature was reduced from 300 K to 30 K. The spin-wave signal weakens, and the group velocity decreases below 30 K. The dependence of spin-wave group velocity on temperature aligns with a change in the YIG saturation magnetization with temperature. Further, we used micromagnetic simulations to shed light on the effect of interlayer dipolar coupling on spin-wave propagation in an FGT/YIG bilayer. In comparison with a single FGT layer, we find an increase in the spin-wave decay length in an FGT/YIG bilayer. Additionally, asymmetric spin-wave dispersion in the FGT/YIG bilayer, induced by chiral dipolar coupling, allows for nonreciprocal control of spin-wave propagation.

2. Experiments

2.1. Film growth and characterization

In the experiment, a 200-nm-thick FGT flake exfoliated from a single crystal was transferred to a 200-nm-thick YIG film grown by pulse laser deposition.[29] The YIG film, with a Gilbert damping constant $\alpha \approx 5 \times 10^{-4}$,[29] provides an ideal material platform for low-loss magnonic devices. FGT crystals, with a Curie temperature above 300 K, have been extensively investigated in terms of structural and magnetic properties. Before device fabrication, the structural and magnetic properties of YIG and FGT were characterized by transmission electron microscopy (TEM), x-ray diffraction (XRD), and a vibrating sample magnetometer (VSM) in a Dynacool physical property measurement system. As shown in Fig. 1(a), the high-resolution cross-sectional TEM image signifies the epitaxial growth of YIG on a GGG(111) substrate. Figure 1(b) presents the VSM hysteresis loops of the YIG film measured at temperatures of 300 K to 10 K. Very small coercive fields in the loops indicate negligible magnetic anisotropy of the YIG film. Figure 1(c) illustrates the crystal structure of FGT with rhombohedral symmetry. Its lattice constants are $a = 0.4$ nm, $b = 0.4$ nm, and $c = 2.9$ nm. Along the c axis, three vdW layers, with a gap size of 0.3 nm, interact mainly via a vdW force. The atoms in each vdW layer, consisting of Fe and Ge sheets sandwiched between Te layers, are bonded tightly via covalent bonds. Figure 1(d) shows the VSM hysteresis loops of the FGT crystal measured at temperatures of 300 K to 10 K. The coercive field increases with decreasing temperature, due to a reduced thermal effect.[30]

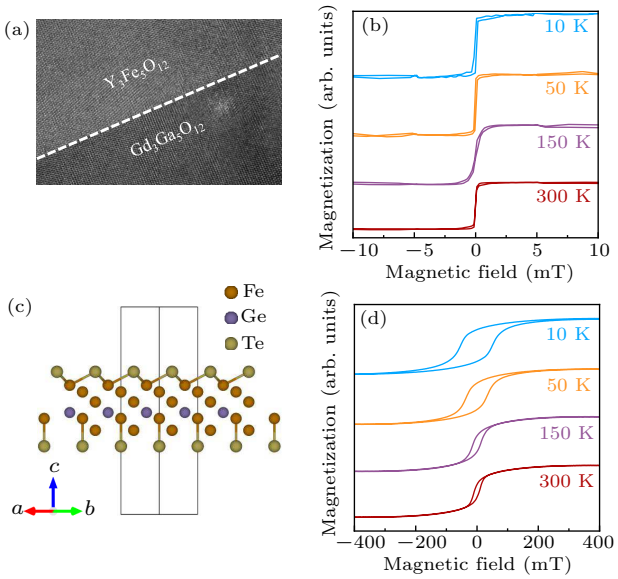


Fig. 1. (a) High-resolution TEM image of a 200-nm-thick YIG film grown on a GGG(111) substrate. The dashed line indicates a sharp interface between the GGG(111) substrate and single-crystal YIG film. (b) Magnetic hysteresis loops measured in the YIG film using a VSM at 10 K, 50 K, 150 K, and 300 K. The magnetic field was applied along the in-plane direction of the film. (c) Side view of the Fe_5GeTe_2 crystal structure. (d) VSM hysteresis loops of Fe_5GeTe_2 measured at 10 K, 50 K, 150 K, and 300 K with a magnetic field applied along the in-plane direction of the crystal.

2.2. Microwave antenna fabrication

We used microwave antennas with widths w to excite and detect spin waves in the YIG and FGT/YIG layers. The antenna is made of shorted ground-signal-ground (GSG) coplanar waveguides, where a narrow stripe that is an antenna connects the signal line to the ground line, as shown in the inset of Fig. 2(a). This type of antenna geometry reduces impedance mismatch and improves the efficiency of spin-wave excitation. We used a laser writer to pattern microwave antennas. Before patterning, the YIG film was cleaned in acetone for 10 min and in isopropanol for 5 min using an ultrasonic bath. A uniform AZ5214 photoresist layer with a thickness of 1 μm was coated using a spinner, followed by a soft bake at 100 °C for 90 s. Direct laser writing was used to write antenna patterns with optimized parameters determined by a dose test process. After exposure, the YIG film was developed in an AZ400K developer and rinsed in deionized water. We used an evaporator to grow 8-nm Cr/100-nm Au, followed by a lift-off in acetone for 30 min.

2.3. The vdW magnet exfoliation and transfer

We used a polydimethylsiloxane (PDMS)/polycarbonate (PC) bilayer transfer stamp to transfer an FGT flake onto a YIG film. The transfer stamp fabrication process is described below. First, a 9.05% PC solution in chloroform was spin-coated onto a glass slide, followed by annealing at 100 °C for 15 s to form a mechanically robust film. Second, the PC film was laminated onto a PDMS block of $1 \times 1 \times 0.5$ mm^3,

using the viscoelasticity of PDMS to buffer interfacial stress during transfer. For thermomechanical pickup, the FGT/SiO_2 substrate was heated to 80 °C to thermally expand the interface, and the PC stamp was aligned and pressed until Newton rings appeared, indicating molecular-level contact. A programmed thermal ramp (0.01 °C/s to 100 °C) exploited the stark thermal expansion mismatch between PC and SiO_2, generating directional stress to exfoliate FGT flakes from the substrate while minimizing wrinkles. The PDMS layer dynamically dissipated residual stress during cooling (0.01 °C/s), preserving flake integrity. Subsequent alignment and release involved heating the YIG film to 180 °C (above PC's glass transition temperature) to activate adhesion. The stamp, bearing FGT, was aligned with submicron precision and pressed onto the YIG surface until Newton rings reappeared, ensuring intimate contact. Controlled vertical retraction at 0.1 mm/s under 180 °C induced edge-initiated peeling of the PC film, enabling the FGT layer to spontaneously adhere to the YIG film via stronger vdW interactions. The residual PC was dissolved by sequential rinsing in chloroform and isopropanol, followed by nitrogen drying. Atomic force microscopy confirmed that the transferred FGT layer exhibited atomic-scale smoothness (RMS < 0.6 nm) and alignment accuracy within ± 200 nm relative to the antenna edge. This bilayer stamp strategy, in combination thermomechanical actuation with viscoelastic stress relief, provides a pathway for integrating air-sensitive 2D magnets into a magnonic architecture while preserving interfacial quality.

3. Results and discussion

We first performed measurements of spin-wave propagation in a 200-nm-thick YIG film without FGT at temperatures of 300 K to 10 K. The inset of Fig. 2(a) shows the measurement geometry, where an external magnetic field ($H_{\rm ext}$, black arrow) was applied parallel to the antenna and perpendicular to the spin-wave wave vector (k). In this configuration, the Damon–Eshbach spin waves or magnetostatic surface spin waves are excited in the YIG film. The distance between the excitation and detection antennas is 10 μm. To measure spin waves in the Montana cryostat, the microwave antennas on the YIG film were electrically connected via wire bonding to the low-temperature stage with two GSG types of electrodes, which are connected to a two-port vector network analyzer (VNA). Figure 2(a) shows spin-wave reflection spectra (imaginary part of S_{22} parameter, referred to as spin-wave excitation at port 2 and detection at port 2 of the VNA), measured from a continuous YIG film for different temperatures. The external magnetic field was 216 mT to ensure a fully saturated YIG film. The FMR mode, corresponding with the deepest dip in the S_{22} spectrum, shifts to high frequency with lowering temperature. The broad peak in the S_{22} spectrum is due to the $0 - 2\pi/w$ excitation range of the microwave antenna, which corresponds to the spin-wave excitation in the frequency range of f ($k = 0$) to f ($k = 2\pi/w$), obtained from the spin-wave dispersion relation. Figure 2(b) shows a change in the frequency of FMR in YIG as a function of temperature. An increase in FMR frequency is observed with the temperature down to about 30 K, due to the enhanced saturation magnetization of YIG at low temperature.[31] Below 30 K, the FMR frequency decreases, which is associated with GGG-induced stray fields.[32] Additionally, a magnetized GGG substrate increases the damping of YIG at low temperature. As shown in Fig. 2(a), the FMR peak at 30 K is broader than the one at 290 K, consistent with the results in the literature.[32,33]

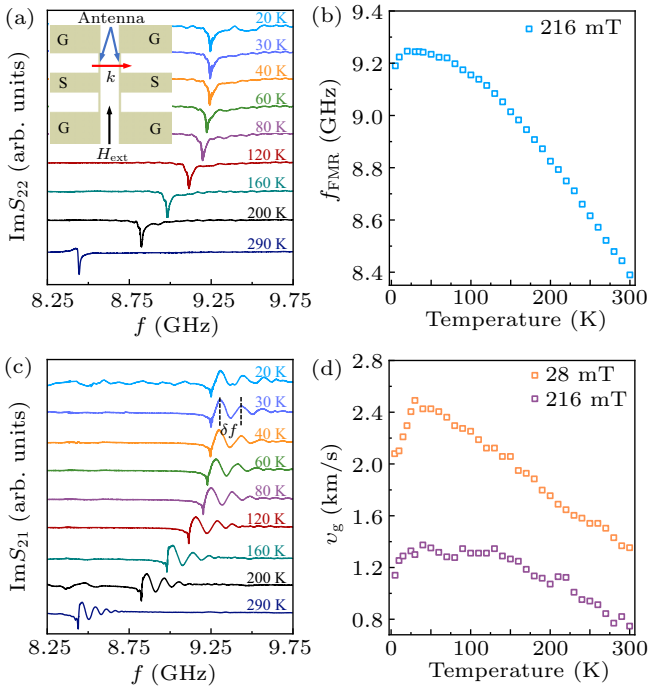


Fig. 2. (a) Temperature-dependent spin-wave reflection spectrum (imaginary part of S_{22}) for a 200-nm-thick YIG film at a magnetic bias field of 216 mT under 0 dBm excitation power. The inset shows a schematic of the microwave antennas for spin-wave excitation and detection. (b) FMR frequency as a function of temperature, extracted from spin-wave reflection spectra. (c) Temperature-dependent spin-wave transmission spectrum (imaginary part of S_{21}) for a 200-nm-thick YIG film at a magnetic bias field of 216 mT. (d) Spin-wave group velocity as a function of temperature at 28 mT and 216 mT, extracted from the frequency spacing between maxima in the ImS_{21} spectrum (see δf in (c)) and the antenna separation s, using $\delta f \times s$.[34]

To investigate spin-wave propagation at low temperature, we recorded the S_{21} spectra (referred to as spin-wave excitation at port 1 and detection at port 2 of the VNA) at temperatures of 300 K to 10 K (Fig. 2(c)). The signal oscillation evidences the transmission of spin waves over 10 μm. Using $v_{\rm g} = \delta f \times s$,[34] where δf is the frequency spacing between two nearest maxima or minima and s is the propagation distance, the spin-wave group velocity $v_{\rm g}$ can be estimated at different magnetic fields and temperatures. With this method, the group velocity in a frequency range of f to $f + \delta f$ is estimated.

Since spin waves cover a wide frequency range, the group velocity at another frequency should be extracted by counting δf at that frequency. Figure 2(d) shows the spin-wave group velocity in the frequency range marked by two dashed lines in Fig. 2(c), as a function of temperature for 28 mT and 216 mT. With decreasing temperature from 300 K to 10 K, υ_g at 28 mT increases from ∼1.4 km/s to ∼2.5 km/s and then drops to ∼ 2 km/s, while it increases from ∼ 0.7 km/s to ∼ 1.4 km/s and then drops to ∼1.2 km/s for 216 mT. The change in spin-wave group velocity with temperature aligns with a change in the YIG saturation magnetization, as shown in Fig. 2(b). This is because a large saturation magnetization yields a steeper dispersion curve, resulting in a higher group velocity. Similarly, a decrease in the group velocity with increasing magnetic field is attributed to the flattening of spin-wave dispersion at high magnetic fields.

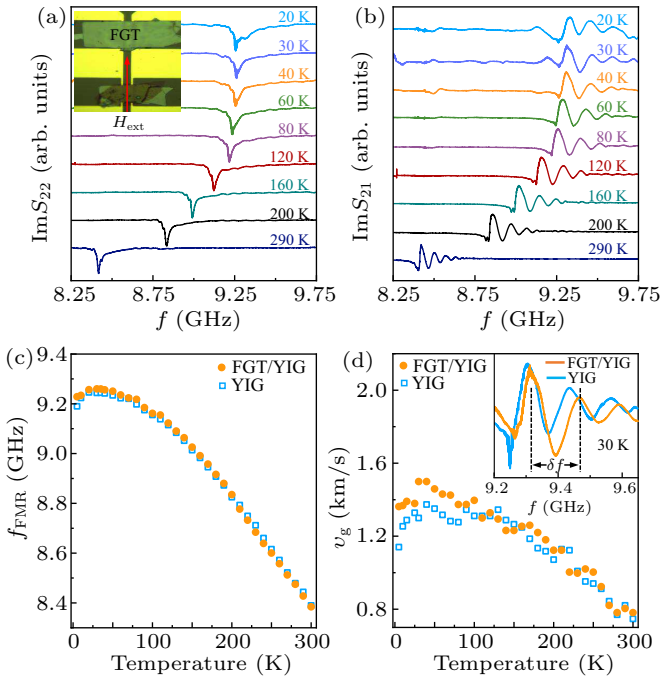


Fig. 3. (a), (b) Temperature-dependent spin-wave reflection spectrum (imaginary part of S_{22}) and spin-wave transmission spectrum (imaginary part of S_{21}), measured from the bilayer of 200-nm-thick FGT layer and 200-nm-thick YIG film at 216 mT under 0 dBm excitation power. The inset shows the image of the FGT/YIG bilayer. (c) FMR of the FGT/YIG bilayer as a function of temperature, extracted from spin-wave reflection spectra. For comparison, the FMR frequency of the YIG film is shown. (d) Spin-wave group velocity in the bilayer as a function of temperature at 216 mT, extracted from spin-wave transmission spectra. For comparison, the group velocity extracted from the YIG film is shown. The inset shows spin-wave transmission spectra measured from the YIG film and FGT/YIG bilayer at 30 K. The dashed lines mark δf in the ImS_{21} spectrum of the FGT/YIG bilayer.

The efficient spin-wave transmission and enhanced group velocity in the YIG film are promising for designing FGT/YIG bilayer devices. Figures 3(a) and 3(b) show the S_{22} and S_{21} spectra measured on a FGT/YIG bilayer at different temperatures. A 216 mT field was applied parallel to the antenna to saturate the YIG and FGT layer (inset of Fig. 3(a)). Figures 3(c) and 3(d) summarize the FMR frequency and spin-wave group velocity as a function of temperature. For comparison, the data shown in Figs. 2(b) and 2(d) (empty squares) are plotted here. As the temperature decreases, both the FMR frequency and group velocity increase, with a maximum at about 30 K. This behavior is similar to that in the YIG film. However, the FMR frequency and group velocity in the FGT/YIG bilayer are higher than those in the YIG film within a temperature range of 100 K to 10 K. As shown in the inset of Fig. 3(d), δf (marked by dashed lines) in the ImS_{21} spectrum measured from the FGT/YIG layer is larger than the one in the YIG layer at 30 K, indicating a higher group velocity in the FGT/YIG layer. A difference in the FMR frequency and spin-wave group velocity signifies the effect of the FGT layer on the spin-wave propagation. Since a difference in the saturation magnetization of FGT and YIG (M_s(FGT)=210 kA/m and M_s(YIG)=181 kA/m) is small, we expect a small change in the FMR and group velocity in the FGT/YIG bilayer.

Next, we used micromagnetic simulations in MuMax3[35] to shed more light on spin-wave propagation in the FGT/YIG bilayer. In the simulations, a single FGT layer with a thickness of 50 nm and a 50-nm FGT/50-nm YIG bilayer are considered. The simulated area is discretized into 4096 × 2 × 16 cells with a cell size of 20 × 20 × 5 nm^3. The reason for simulating a 50-nm-thick FGT layer is that a thinner vdW magnet is more attractive for magnonics. However, the spin-wave signal in a thin FGT layer is too weak to be measured using broadband spin-wave spectroscopy in our study. To mimic a continuous layer, the periodic boundary condition was applied along the y axis. A 200-nm-wide region with $\alpha = 0.5$ was added at both ends of the x direction to minimize spin-wave reflection from the edge of the film. The material parameters for FGT ($M_s = 210$ kA/m, $A_{ex} = 9$ pJ/m, $K_u = 211.7$ J/m^3, $\alpha = 0.04$) were taken from the literature.[20] The input YIG parameters are $M_s = 181$ kA/m, $A_{ex} = 3.1$ pJ/m, $K_u = 0$ J/m^3, and $\alpha = 0.001$. The interlayer interaction between two vdW layers is not considered because a MuMax3 simulation of a 0.3 nm vdW gap is impossible for our computers. A 0.1-mT ac excitation field applied in a 100-nm-wide area centering at $x = 0$ and through the thickness along the z axis was used to locally excite spin waves. The external magnetic fields of 216 mT and 22.5 mT were applied along the y axis to establish a Damon–Eshbach configuration. We recorded m_z for a total simulation time of 240 ns.

Figures 4(a) and 4(b) show simulated spatial images of spin-wave propagation (m_z) in a 50-nm-thick FGT layer at 216 mT and 22.5 mT. The spin-wave frequencies are 10.47 GHz and 3.87 GHz, respectively. From the images, we find the spin waves propagate along the $\pm x$ directions with nearly the same intensity, indicating reciprocal propagation. By extracting the wavelength $\lambda = 2\pi/k$, where k is the wave vector, the dispersion relations at 216 mT and 22.5 mT are

plotted in Fig. 4(c). For comparison, the spin-wave dispersion in a 50-nm-thick YIG film (dashed lines) is also plotted, which is calculated using the formula of Slavin and Kalinikos.[36] All dispersion curves are symmetric with respect to the wave vectors. Compared to the YIG film, the spin-wave dispersion in FGT shifts to the higher frequency, due to the higher M_s. By fitting the data in Figs. 4(a) and 4(b) to the formula of $A\,e^{-x/l_d}\sin(x)$, the spin-wave decay length l_d is extracted at different frequencies, as shown in Fig. 4(d). The l_d in the FGT layer (solid squares) is less than 0.6 μm for 22.5 mT and 0.15 μm for 216 mT in the full excitation range, which is much shorter than l_d in the YIG film (solid circles), calculated using $l_d = \upsilon_g/(2\pi\alpha f)$. The short spin-wave decay length in FGT, arising from its high damping, limits the spin-wave propagation to a few micrometers, as shown in Figs. 4(a) and 4(b).

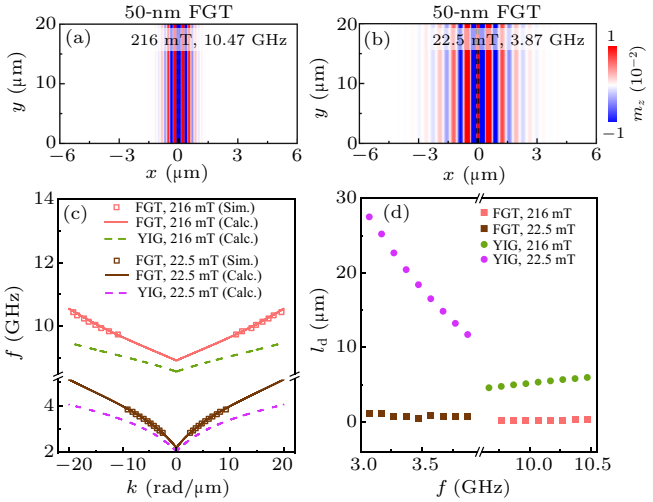


Fig. 4. (a), (b) Micromagnetic simulations on the spin-wave propagation in a 50-nm-thick FGT layer at 216 mT and 22.5 mT. The spin waves of 10.47 GHz and 3.87 GHz are excited with a 0.1-mT ac field applied in a 100-nm-wide region centering at $x = 0$. (c) Simulated spin-wave dispersion relations in a 50-nm-thick FGT layer (empty squares) at 216 mT and 22.5 mT. The solid and dashed lines represent calculated dispersion relations in the 50-nm-thick FGT and YIG layers at 216 mT and 22.5 mT, respectively. (d) Spin-wave decay lengths in a 50-nm-thick FGT layer (squares) and 50-nm-thick YIG (circles) at 216 mT and 22.5 mT.

We now turn to the simulations on the FGT/YIG bilayer. Figures 5(a)–5(d) present simulated spatial maps of spin-wave propagation in the bilayer of 50-nm-thick FGT and 50-nm-thick YIG at 216 mT and 22.5 mT. Note that the wave profiles in the FGT and YIG layers are the same, but with different amplitudes. Here, the m_z component in the FGT layer is plotted. The 3.37 GHz spin wave propagates over several micrometers at 22.5 mT (Fig. 5(a)), which is nearly one order of magnitude longer than that in a single FGT layer. At higher frequencies, the spin-wave propagation along the $\pm x$ direction becomes rather distinct, indicating a nonreciprocal character. For example, the 3.87 GHz spin wave has a wavelength of $\lambda = 758$ nm in the $-x$ ($-k$) direction and $\lambda = 312$ nm in the $+x$ ($+k$) direction. Moreover, the propagation distance in the $-x$ direction is shorter than in the $+x$ direction. For the case of 216 mT (Figs. 5(c) and 5(d)), the propagation distance of the 9.67 GHz spin wave is shorter than the 10.47 GHz spin wave, which also indicates nonreciprocal propagation along the $\pm x$ axis. Figure 5(e) shows the spin-wave decay length l_d for 216 mT and 22.5 mT, obtained by fitting the wave profiles to $A\,e^{-x/l_d}\sin(x)$. For 216 mT, the decay length increases from ∼0.5 μm to ∼1 μm for $+k$ (solid squares) and from ∼0.2 μm to ∼0.5 μm for $-k$ (empty squares), with increasing frequency. For 22.5 mT, the decay lengths of spin waves with $\pm k$ decrease from ∼3.5 μm to ∼0.5 μm, and then increase with frequency. Notably, the decay length reaches a minimum near 3.87 GHz for $+k$ spin waves and near 4.25 GHz for $-k$ spin waves. To explain this phenomenon, simulated spin-wave dispersion relations in the bilayer are shown in Fig. 5(f). At 216 mT, a parabolic-like dispersion curve (blue squares) is observed at large wave vectors. At 22.5 mT, the dispersion curve (orange squares) is steep at $k < 10$ rad/μm and then becomes flat in the range of 10 rad/μm $< k <$ 20 rad/μm. The curves steepens again for $k > 20$ rad/μm. In contrast, the dispersion of spin waves with $-k$ does not show a flatness in the range of -10 rad/μm to -20 rad/μm. By deriving the dispersion relation, Fig. 5(h) shows the spin-wave group velocity υ_g (squares), e.g., $\upsilon_g = 0.24$ km/s at $k = -12.5$ rad/μm, and $\upsilon_g = 0.1$ km/s at

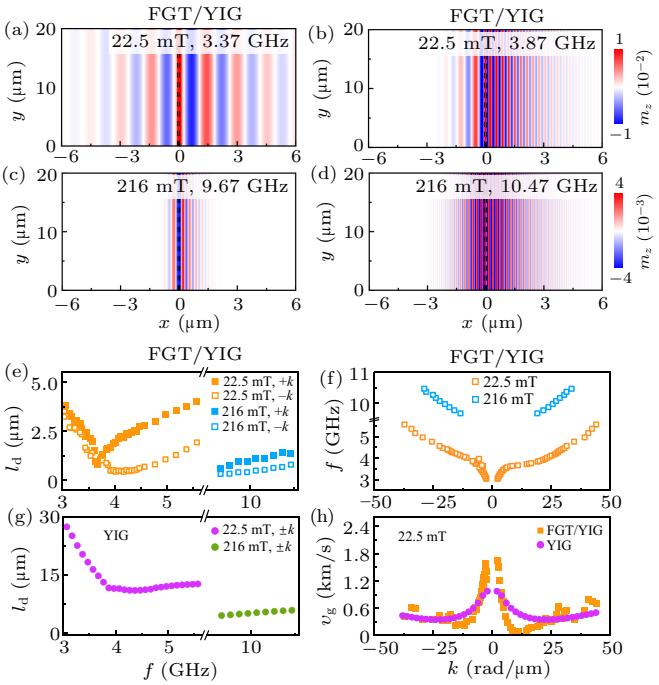


Fig. 5. (a)–(d) Micromagnetic simulations on spin-wave propagation in the bilayer of 50-nm-thick FGT/50-nm-thick YIG at external magnetic fields of 22.5 mT (a), (b) and 216 mT (c), (d), excited by a 100-nm-wide antenna centering at $x = 0$. The spin-wave propagations at frequencies of 3.37 GHz (a), 3.87 GHz (b), 9.67 GHz (c), and 10.47 GHz (d) are shown. (e) Simulated spin-wave decay length in the FGT/YIG bilayer as a function of frequency at 22.5 mT and 216 mT. The solid and empty squares represent the decay lengths of spin waves with $+k$ and $-k$, respectively. (f) Spin-wave dispersion relations in the bilayer at 22.5 mT and 216 mT. (g) Simulated spin-wave decay length in a 50-nm-thick YIG film as a function of frequency at 22.5 mT and 216 mT. (h) Spin-wave group velocity in the FGT/YIG bilayer (squares) and the YIG film (circles) at 22.5 mT.

$k = +12.5$ rad/μm at 22.5 mT. From this, we expect the longer decay length at $-k$ than that at $+k$ for the 3.87 GHz spin wave. However, it is opposite to the simulation. As a comparison, Fig. 5(g) shows spin-wave decay length in a 50-nm-thick YIG film for 216 mT and 22.5 mT. It is seen that the decay length in the FGT/YIG bilayer (Fig. 5(e)) is nearly one order of magnitude shorter than that in the YIG film. Since spin-wave group velocity in FGT/YIG is comparable to the YIG film (Fig. 5(h)), the shorter decay length in FGT/YIG is attributed to the higher Gilbert damping. This indicates integration of FGT with YIG enhances the propagation of spin waves in the FGT layer at the expense of reducing the decay length in the YIG film.

To reveal underlying physics, we simulated spin-wave propagation in the FGT/YIG bilayer with varying damping constant of FGT. The YIG damping constant in the bilayer is fixed at 0.001. Figures 6(a) and 6(b) show the spin-wave decay length as a function of α_{FGT} at 3.37 GHz and 3.87 GHz. With increasing α_{FGT} from 0.001 to 0.04, the decay lengths of the 3.37 GHz spin waves with $-k$ and $+k$ reduce from 68 μm to 2 μm. The long decay length in the FGT/YIG layer with a low damping constant, e.g., $\alpha = 0.001$, confirms the integration of high-damping FGT with low-damping YIG increases the spin-wave decay length in FGT, but reduces the decay length in YIG.

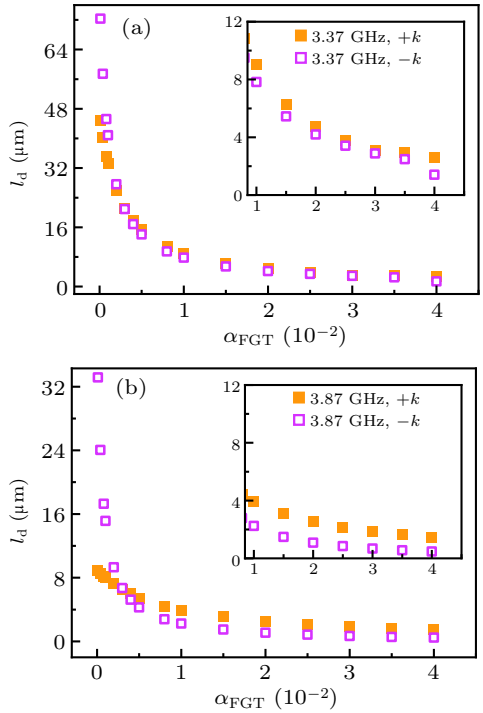


Fig. 6. (a) Decay length of the 3.37 GHz spin wave as a function of FGT damping constant in the bilayer. The solid and empty squares represent the decay length of the 3.37 GHz spin wave with $+k$ and $-k$, respectively. The inset shows a zoom-in of the data. (b) The same plot as in (a), but for 3.87 GHz spin waves.

In contrast, the decay length of the 3.87 GHz spin wave with $+k$ is much shorter than that with $-k$ when $\alpha_{\mathrm{FGT}} < 0.003$, while it becomes longer when $\alpha_{\mathrm{FGT}} > 0.003$ (see the inset of Fig. 6(b)). As the decay length l_{d} is determined by υ_{g} and α, the υ_{g} at $k = 12.5$ rad/μm (corresponding to 3.87 GHz) is less than that at $k = -12.5$ rad/μm (Fig. 5(h)), the effective damping at $k = 12.5$ rad/μm should be lower than that at $k = -12.5$ rad/μm. This suggests nonreciprocal effective damping, which may arise from strong spin-wave interaction in the region of flat dispersion (Fig. 5(f)), where abundant spin-wave states coexist with nearly the same frequency but different wave vectors.

4. Conclusion

In summary, we experimentally and numerically investigated spin-wave propagation in a bilayer material system consisting of low-damping YIG and high-damping FGT films. We revealed the dependence of spin-wave parameters, e.g., decay length and group velocity on frequency and wave vector, as well as temperature and magnetic field. At low temperature, an increase in the spin-wave group velocity and nonreciprocal spin-wave propagation with long decay length were observed in the bilayer. We further investigated the tuning of the spin-wave decay length by varying the Gilbert constant and demonstrated nonreciprocal effective magnetic damping in the bilayer. These attributes are ascribed to dynamical dipolar coupling in the FGT/YIG bilayer, which leads to asymmetric spin-wave dispersion relations and nonreciprocal propagation. Our results pave the way for the design of low-loss magnonic devices with controllable properties based on vdW magnetic materials.

Acknowledgements

This work was supported by the National Key Research and Development Program of China (Grant No. 2022YFA1402400) and the National Natural Science Foundation of China (Grant No. 12374119). We thank the support of the Center for Nanoscience and Nanotechnology and the Supercomputing Center at Wuhan University in China.

References

[1] Burch K S, Mandrus D and Park J G 2018 *Nature* **563** 47
[2] Gibertini M, Koperski M, Morpurgo A F and Novoselov K S 2019 *Nat. Nanotechnol.* **14** 408
[3] Jiang X, Liu Q, Xing J, Liu N, Guo Y, Liu Z and Zhao J 2021 *Appl. Phys. Rev.* **8** 031305
[4] Liu N S, Wang C and Ji W 2022 *Acta Phys. Sin.* **71** 127504 (in Chinese)
[5] Zhang B, Lu P, Tabrizian R, Feng P X L and Wu Y 2024 *npj Spintronics* **2** 6
[6] Huang B, Clark G, Navarro-Moratalla E, Klein D R, Cheng R, Seyler K L, Zhong D, Schmidgall E, McGuire M A, Cobden D H, Yao W, Xiao D, Jarillo-Herrero P and Xu X 2017 *Nature* **546** 270
[7] Gong C, Li L, Li Z, Ji H, Stern A, Xia Y, Cao T, Bao W, Wang C, Wang Y, Qiu Z Q, Cava R J, Louie S G, Xia J and Zhang X 2017 *Nature* **546** 265
[8] Mermin N D and Wagner H 1966 *Phys. Rev. Lett.* **17** 1133
[9] Soumyanarayanan A, Reyren N, Fert A and Panagopoulos C 2016 *Nature* **539** 509

[10] Kajiwara Y, Harii K, Takahashi S, Ohe J, Uchida K, Mizuguchi M, Umezawa H, Kawai H, Ando K, Takanashi K, Maekawa S and Saitoh E 2010 *Nature* **464** 262

[11] Khitun A, Bao M and Wang K L 2010 *J. Phy. D: Appl. Phys.* **43** 264005

[12] Chumak A V, Vasyuchka V, Serga A and Hillebrands B 2015 *Nat. Phys.* **11** 453

[13] Chumak A V, Kabos P, Wu M, *et al.* 2022 *IEEE Trans. Magn.* **58** 1

[14] Zhang X X, Li L, Weber D, Goldberger J, Mak K F and Shan J 2020 *Nat. Mater.* **19** 838

[15] Cenker J, Huang B, Suri N, Thijssen P, Miller A, Song T, Taniguchi T, Watanabe K, McGuire M A, Xiao D and Xu X 2020 *Nat. Phys.* **17** 20

[16] Shen X, Chen H, Li Y, Xia H, Zeng F, Xu J, Kwon H Y, Ji Y, Won C, Zhang W and Wu Y 2021 *J. Magn. Magn. Mater.* **528** 167772

[17] MacNeill D, Hou J T, Klein D R, Zhang P, Jarillo-Herrero P and Liu L 2019 *Phys. Rev. Lett.* **123** 047204

[18] Xu H, Jia K, Huang Y, Meng F, Zhang Q, Zhang Y, Cheng C, Lan G, Dong J, Wei J, Feng J, He C, Yuan Z, Zhu M, He W, Wan C, Wei H, Wang S, Shao Q, Gu L, Coey M, Shi Y, Zhang G, Han X and Yu G 2023 *Nat. Commun.* **14** 3824

[19] Alahmed L, Nepal B, Macy J, Zheng W, Casas B, Sapkota A, Jones N, Mazza A R, Brahlek M, Jin W, Mahjouri-Samani M, Zhang S S L, Mewes C, Balicas L, Mewes T and Li P 2021 *2D Mater.* **8** 045030

[20] Schulz F, Litzius K, Powalla L, Birch M T, Gallardo R A, Satheesh S, Weigand M, Scholz T, Lotsch B V, Schütz G, Burghard M and Wintz S 2023 *Nano Lett.* **23** 10126

[21] Bae Y J, Wang J, Scheie A, Xu J, Chica D G, Diederich G M, Cenker J, Ziebel M E, Bai Y, Ren H, Dean C R, Delor M, Xu X, Roy X, Kent A D and Zhu X 2022 *Nature* **609** 282

[22] Xing W, Qiu L, Wang X, Yao Y, Ma Y, Cai R, Jia S, Xie X C and Han W 2019 *Phys. Rev. X* **9** 011026

[23] Chen J, Yuan R, Yu K, Wang X, Sheng L, Wang J, Hua C, Yu W, Xiao J, Liu S, Yu D, Ansermet J P, Wang Z and Yu H 2025 *Appl. Phys. Rev.* **12** 011407

[24] Chen G, Qi S, Liu J, Chen D, Wang J, Yan S, Zhang Y, Cao S, Lu M, Tian S, Chen K, Yu P, Liu Z, Xie X C, Xiao J, Shindou R and Chen J H 2021 *Nat. Commun.* **12** 6279

[25] Qi S, Chen D, Chen K, Liu J, Chen G, Luo B, Cui H, Jia L, Li J, Huang M, Song Y, Han S, Tong L, Yu P, Liu Y, Wu H, Wu S, Xiao J, Shindou R, Xie X C and Chen J H 2023 *Nat. Commun.* **14** 2526

[26] Zhang Z, Gao F Y, Curtis J B, Liu Z J, Chien Y C, von Hoegen A, Wong M T, Kurihara T, Suemoto T, Narang P, Baldini E and Nelson K A 2024 *Nat. Phys.* **20** 801

[27] Wu D, Xu Y, Ye M and Duan W 2025 *Sci. Adv.* **11** eadu6562

[28] Hauser C, Richter T, Homonnay N, Eisenschmidt C, Qaid M, Deniz H, Hesse D, Sawicki M, Ebbinghaus S G and Schmidt G 2016 *Sci. Rep.* **6** 20827

[29] Qin H, Hämäläinen S J, Arjas K, Witteveen J and van Dijken S 2018 *Phys. Rev. B* **98** 224422

[30] Ma X, Li R, Zheng B, Huang L, Zhang Y, Wang S, Wang C, Tan H, Lu Y and Xiang B 2023 *Nano Lett.* **23** 11226

[31] Solt Irvin H J 1962 *J. Appl. Phys.* **33** 1189

[32] SSerha R O, Voronov A A, Schmoll D, Verba R, Levchenko K O, Koraltan S, Davídková K, Budinská B, Wang Q, Dobrovolskiy O V, Urbánek M, Lindner M, Reimann T, Dubs C, Gonzalez-Ballestero C, Abert C, Suess D, Bozhko D A, Knauer S and Chumak A V 2024 *npj Spintronics* **2** 29

[33] Kosen S, van Loo A F, Bozhko D A, Mihalceanu L and Karenowska A D 2019 *APL Mater.* **7** 101120

[34] Liu C, Chen J, Liu T, Heimbach F, Yu H, Xiao Y, Hu J, Liu M, Chang H, Stueckler T, Tu S, Zhang Y, Zhang Y, Gao P, Liao Z, Yu D, Xia K, Lei N, Zhao W and Wu M 2018 *Nat. Commun.* **9** 738

[35] Vansteenkiste A, Leliaert J, Dvornik M, Helsen M, Garcia-Sanchez F and Van Waeyenberge B 2014 *AIP Adv.* **4** 107133

[36] Kalinikos B and Slavin A 1986 *J. Phys. C: Solid State Phys.* **19** 7013